

# Optical detection of the black widow binary PSR J2052+1219

S. Zharikov<sup>1\*</sup>, A. Kirichenko<sup>1,2</sup>, D. Zyuzin<sup>2</sup>, Yu. Shibano<sup>2,3</sup> and J. S. Deneva<sup>4</sup>

<sup>1</sup>*Instituto de Astronomía, Universidad Nacional Autónoma de México, Apdo. Postal 877, Ensenada, Baja California, México, 22800*

<sup>2</sup>*Ioffe Institute, 26 Politekhmicheskaya st., St. Petersburg 194021, Russia*

<sup>3</sup>*Peter the Great St. Petersburg Polytechnic University, Politekhmicheskaya 29, St. Petersburg, 195251, Russia*

<sup>4</sup>*George Mason University, resident at the Naval Research Laboratory, 4555 Overlook Ave. SW, Washington, DC 20375, USA*

Accepted 2019 August 30. Received 2019 August 12, in original form 2019 May 21

## ABSTRACT

We present optical time-resolved multi-band photometry of the black widow binary millisecond pulsar J2052+1219 using direct-imaging observations with the 2.1m telescope of Observatorio Astronomico Nacional San Pedro Mártir, Mexico (OAN-SPM). The observations revealed a variable optical source whose position and periodicity  $P = 2.752h$  coincide with the pulsar coordinates and the orbital period obtained from radio timing. This allowed us to identify it with the binary companion of the pulsar. We reproduce light curves of the source modelling the companion heating by the pulsar and accounting for the system parameters obtained from the radio data. As a result, we independently estimate the distance to the system of 3.94(16) kpc, which agrees with the dispersion measure distance. The companion star size is 0.12–0.15  $R_{\odot}$ , close to filling its Roche lobe. It has a surface temperature difference of about 3000 K between the side facing the pulsar and the back side. We summarise characteristics of all black widow systems studied in the optical and compare them with the PSR J2052+1219 parameters derived from our observations.

**Key words:** stars: neutron – pulsars: individual (PSR J2052+1219; PSR J2052+1218) – binaries: close

## 1 INTRODUCTION

Millisecond pulsars (MSPs) form a class of old neutron stars (NSs) that are characterised by short and stable rotational periods  $P$  with typical  $P < 30$  ms and  $\dot{P} \lesssim 10^{-19}$  s s<sup>-1</sup>. It is generally accepted that MSPs are “recycled” by accretion of matter from their main-sequence companions (Bisnovatyi-Kogan & Komberg 1974; Alpar et al. 1982).

Based on the type of the companion star, binary MSPs are divided into several subclasses. Those MSPs bounded in tight orbits (binary periods  $P_b < 20$  h) with very low-mass companions ( $M_c < 0.05 M_{\odot}$ ) are dubbed black widow (BW) pulsars. In these systems, the companion star is ablated by the pulsar high-energy radiation and the wind of relativistic particles until eventually may become fully evaporated. Isolated MSPs that are not associated with globular clusters are believed to be formed in this scenario (van den Heuvel & van Paradijs 1988). They currently account about 20 per cent of the total MSP population<sup>1</sup>.

The first BW system, PSR 1957+20, was introduced

by Fruchter, Stinebring, & Taylor (1988). It is a MSP binary with  $P_b = 9.2$  h and the companion mass  $M_c < 0.05 M_{\odot}$ . Following this discovery, two more BW systems in the Galactic disk, PSR J2051–0827 and PSR J0610–2100, were detected in the *Parkes* radio surveys (Stappers et al. 1996; Burgay et al. 2006). However, no significant progress in the field was made until the launch of the *Fermi* Large Area Telescope. The *Fermi* detections and radio follow-up searches have significantly expanded the general population of observed MSPs<sup>2</sup>, and, as a particular contribution, they increased the amount of known Galactic disk BWs from three to more than twenty<sup>3</sup> (see, e.g., Ray et al. (2012); Cromartie et al. (2016); Bassa et al. (2017) and references therein).

These discoveries, in turn, opened up the possibility for multiwavelength studies of BW systems including the optical range. However, to date only a small fraction of new BWs has been studied in the optical (Wadiasingh et al. 2015). Photometric information was reported for about a

\* E-mail: zhar@astro.unam.mx

<sup>1</sup> <http://astro.phys.wvu.edu/GalacticMSPs/>

<sup>2</sup> <https://fermi.gsfc.nasa.gov/science/etev/pulsars/>

<sup>3</sup> [www.atnf.csiro.au/people/pulsar/psrcat/](http://www.atnf.csiro.au/people/pulsar/psrcat/), Manchester et al. (2005)

**Table 1.** Parameters of PSR J2052+1219.

Observed						Derived				
$P$	$\dot{P}$	$DM$	$l$	$b$	RA	DEC	$P_b$	$\tau$	$B$	$\dot{E}$
ms	$10^{-21}$	$\text{cm}^{-3} \text{ pc}$	( $^\circ$ )	( $^\circ$ )	(J2000)	(J2000)	h	Gyr	G	$\text{erg s}^{-1}$
1.99	6.7	42	59	-20	20:52:47.77844(5)	12:19:59.0281(9)	2.75	4.7	$1.2 \times 10^8$	$3.34 \times 10^{34}$
Orbital Period (d)		semi-major axis (lt-s)			mass function ( $10^{-6} M_\odot$ )			Reference		
0.155		0.061			18.43			Guillemot, et al. (2019)		

dozen of known Galactic disk BWs and only two systems, PSR J1311–3430 and PSR J1301+0833, were studied using spectroscopy (Romani et al. 2012, 2015, 2016). Optical observations of BWs are important to track their evolution and to study the evaporation process and formation of isolated MSPs. In addition, they allow us to set independent constraints on fundamental parameters of these binary systems.

The millisecond PSR J2052+1218 was recently discovered in the Arecibo telescope search of unidentified gamma-ray sources from the *Fermi* Large Area Telescope (LAT) four year point source catalogue (Cromartie et al. 2016). Its coordinates obtained from subsequent radio timing measurements are  $RA_{2000} = 20:52:47.77844(5)$  and  $Dec_{2000} = 12:19:59.0281(9)$ . We will hereafter refer to this pulsar as PSR J2052+1219. The pulsar spin period is  $P=1.99$  ms with  $\dot{P} = 6.7 \times 10^{-21}$ , its characteristic age is  $\tau = 4.7$  Gyr, and the spin-down luminosity is  $\dot{E} = 3.34 \times 10^{34} \text{ erg s}^{-1}$  for a NS moment of inertia of  $I = 10^{45} \text{ g cm}^2$ . It is found in an eclipsing binary system with  $P_b \approx 2.8$  h containing a very low-mass companion (Table 1). Using Keplerian parameters derived from orbital timing solution, Cromartie et al. (2016) have calculated a minimum companion mass of  $\gtrsim 0.033 M_\odot$  suggesting the system is a BW. Based on the dispersion measure  $DM=42 \text{ pc cm}^{-3}$  and the NE2001 Galactic electron-density model (Cordes & Lazio 2002), they estimated a distance to PSR J2052+1219 of 2.4 kpc. However, the pulsar distance based on the YMW16 electron-density model (Yao et al. 2017) is about 3.92 kpc. Accounting for a large Galactic latitude of the pulsar,  $b \approx -20^\circ$ , at such distances it has to be located about 1 kpc above the Galactic disk. This implies a low interstellar extinction in its direction. Indeed, according to the Galactic 3D extinction/distance maps<sup>4</sup>, the reddening along its line of sight reaches an upper limit of  $E(B - V) = 0.12^{+0.02}_{-0.02}$  and remains constant at distances  $\gtrsim 1.5$  kpc. The older measurements<sup>5</sup> give slightly smaller values of the total Galactic absorption in the pulsar direction:  $E(B - V) = 0.0844 \pm 0.0053$  (Schlafly & Finkbeiner 2011) and  $E(B - V) = 0.0981 \pm 0.0062$  (Schlegel, Finkbeiner, & Davis 1998). Therefore, taking into account the uncertainties, below we consider the colour excess at the pulsar distance to be in a range of  $E(B - V) = 0.08 - 0.14$ .

Inspection of the Panoramic Survey Telescope and Rapid Response System Survey (Pan-STARRS; Flewelling et al. (2016)) catalogue allowed us to reveal a possible optical counterpart of the pulsar companion, PSO

**Table 2.** Log of the PSR J2052+1219 observations with the 2.1m telescope at the OAN-SPM.

Date	Filter	Exposure time, seconds	Airmass	Seeing, arcsec
14/09/2018	R	600x38	1.1–2.2	1.4–2.2
15/09/2018	R	600x34	1.1–1.7	1.5–2.4
16/09/2018	V	600x16	1.1–1.2	1.5–1.8
17/09/2018	R	600x16	1.1–1.6	1.4–1.7
	B	600x2	1.4–1.5	1.5–1.6
	V	600x2	1.4–1.7	1.4–1.5
	R	600x28	1.1–1.8	1.5–1.6
	I	600x2	1.5–1.9	1.3–1.5

**Table 3.** Secondary photometric standards marked in Fig. 1.

Star	B	V	R	I
A	20.95(1)	19.71(1)	18.97(2)	18.43(2)
B	19.65(1)	18.95(1)	18.52(1)	18.12(1)
C	19.40(1)	18.40(1)	17.80(1)	17.23(1)
D	19.51(1)	18.55(1)	17.95(1)	17.31(1)

J205247.782+121959.174, with  $r' \approx 22.3$ . To confirm it and determine the physical parameters of the source, we performed optical time-resolved multi-band observations.

## 2 OBSERVATIONS AND DATA REDUCTION

The time-resolved photometric observations of the pulsar field were performed with the "Rueda Italiana" instrument<sup>6</sup> attached to the 2.1m telescope at the Observatorio Astronómico Nacional San Pedro Mártir (OAN-SPM), Mexico on September 14–17, 2018. The field of view of the detector was  $6' \times 6'$  with an image scale of  $0''.34$  in the  $2 \times 2$  CCD pixel binning mode. The conditions during the observing run were clear. The observing log is presented in Table 2.

We carried out standard data processing, including bias subtraction and flat-fielding with the Image Reduction and Analysis Facility (IRAF) package. The cosmic rays were removed from all images using the L.A.Cosmic algorithm (van Dokkum 2001). Astrometric referencing was performed on a single 600s exposure obtained in the best-seeing conditions. We used a set of 9 stars from the Gaia DR2 Catalogue (Gaia Collaboration et al. 2016, 2018) with positional errors

<sup>4</sup> <http://argonaut.skymaps.info><sup>5</sup> <https://irsa.ipac.caltech.edu/applications/DUST/><sup>6</sup> [www.astrosen.unam.mx](http://www.astrosen.unam.mx)

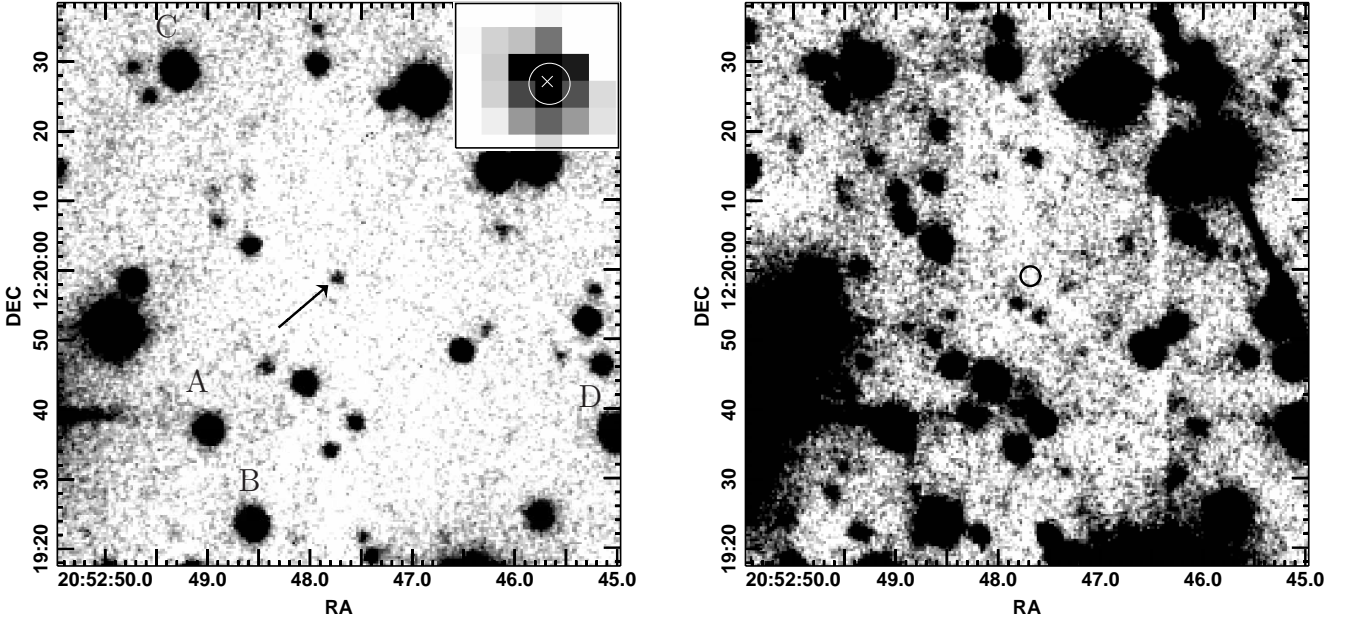


**Figure 1.** *Left panel:*  $\approx 1.3' \times 1.3'$  image of the PSR J2052+1219 field obtained in the *R*-band. The arrow points to the variable source located at the pulsar radio position. It is enlarged in the top-right corner. The cross shows its centre on the image and the circle corresponds to the  $3\sigma$  pulsar radio timing position uncertainty. The letters mark the secondary photometric standards in the pulsar field from Table 3. The image corresponds to the object’s peak brightness. *Right panel:* Deeper image of the same field in the same band obtained near the minimum brightness stage of the same source when it falls below the detection limit. The source position is marked by the circle.

of  $\lesssim 0.13$  mas. Formal *rms* uncertainties of the resulting astrometric fit were  $\Delta RA \lesssim 0''.09$  and  $\Delta Dec \lesssim 0''.07$ . The catalogue conservative uncertainty of 0.7 mas (Lindgren et al. 2018) can be neglected in case of our astrometric solution.

The photometric calibration was performed using reference stars from the PG2213–006 standard field (Landolt 1992) observed on September 17, 2018 immediately after the target. Using their instrumental magnitudes and the site extinction coefficients  $k_B=0.25$ ,  $k_V=0.14$ ,  $k_R=0.07$  and  $k_I=0.06$  (Schuster & Parrao 2001; Schuster et al. 2002), we calculated the zero-points for this night:  $Z_B^L=24.88 \pm 0.01$ ,  $Z_V^L=25.15 \pm 0.01$ ,  $Z_R^L=25.00 \pm 0.01$  and  $Z_I^L=24.20 \pm 0.01$ . The zero-points were verified using  $\sim 20$  stars in the target field whose magnitudes were extracted from the Pan-STARRS catalogue. The Pan-STARRS *gri* magnitudes (Tonry et al. 2012) were transformed to the *BVRI* system using the equations (1–7) and coefficients from Table 2 of Kostov & Bonev (2018). Using the obtained values, we then calculated the zero-points  $Z_B^P=24.78 \pm 0.01$ ,  $Z_V^P=25.05 \pm 0.01$ ,  $Z_R^P=24.83 \pm 0.01$  and  $Z_I^P=24.13 \pm 0.01$ . We found a “grey” shift of  $\approx 0.10$  between the  $Z^L$  and  $Z^P$  values. Revising several field stars on different time-resolved images, we found a slight transparency variation of about 0.1 mag. Therefore, in the following analyses we only use the  $Z^P$  values.

To calibrate the data obtained during the other nights, we measured magnitudes of four stars in the pulsar vicinity, which we defined as secondary photometric standards. They are marked in the left panel of Fig. 1 with A, B, C and D, and their magnitudes are given in Table 3.

### 3 RESULTS

The *R*-band images of the pulsar field are presented on both panels of Fig. 1. The arrow on the left panel points towards a source which shows strong variability. It is clearly visible on several subsequent images and is absent on others obtained during the same night. The  $\sim 2'' \times 2''$  vicinity of the object is enlarged in the top-right corner of the left panel, and its peak position is shown by the white cross. The centre of the circle corresponds to the pulsar radio position. The circle radius of  $0.27''$  represents the  $3\sigma$  pulsar radio position uncertainty that accounts for the optical astrometric referencing and the radio timing uncertainties.

The source and the pulsar positions coincide perfectly, suggesting their association. We performed time-resolved aperture photometry of the source. The object magnitude at the maximum is  $R_c \approx 22.0$ , whereas on some other images the brightness of the source falls below the  $3\sigma$  detection limit<sup>7</sup>  $R_c^{\text{lim}} \sim 24.1$  of a single 600 s exposure.

The obtained *R*-band photometric data were analysed to search for periodicity using the Discrete Fourier Transform code (Deeming 1975). The resulting power spectrum is presented on the top panel of Fig. 2. The peak corresponding to the maximum power yields the photometric period of  $P_{\text{phot}} = 2.752$  h, which is in agreement with the pulsar binary period  $P_b = 2.75$  h (Thankful Cromartie, private communication). The light curves folded with the pho-

<sup>7</sup> The detection limits presented in this article were derived following the standard procedure (see, e.g., Zharikov & Mignani (2013)).

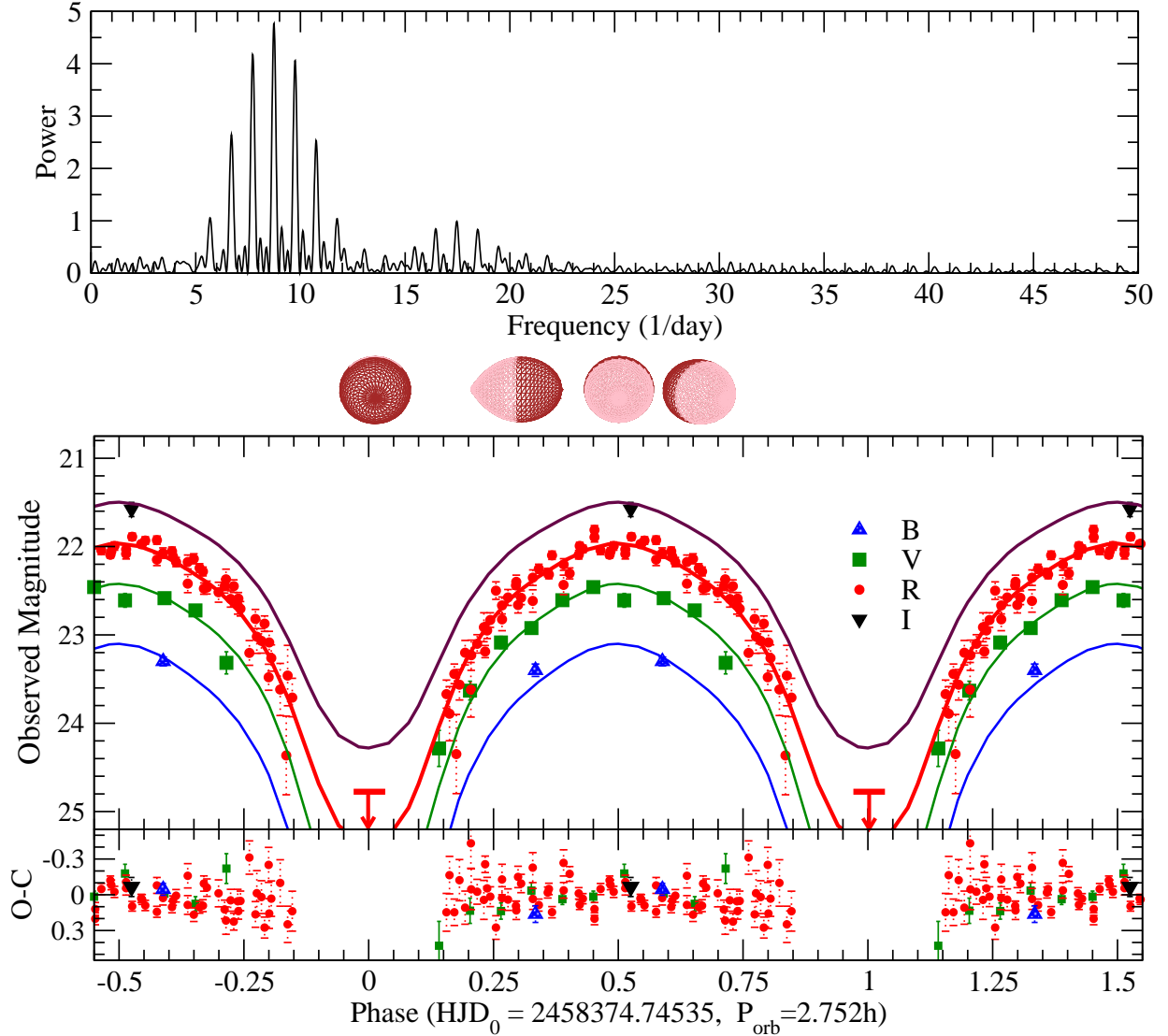


**Figure 2.** Upper panel: Power spectrum of the variable source based on the *R*-band data. The main peak corresponds to an orbital period of 2.752 h. Lower panel, top: Observed *BVRI* light curves of the source folded with the orbital period and best fits to the data (solid lines) using the model described in the text. Two periods corresponding to the orbital phase range -0.5–1.5 are shown for clarity. The model shapes of the secondary and the brightness distribution over its surface as visible by an observer at phases 0.0, 0.25, 1.0 and 1.125 are shown at the top of the plot. Lower panel, bottom: The observed minus calculated (O-C) light curves.

tometric period are shown in the bottom panel of Fig. 2. The phase 0.0, defined as the time when the secondary is placed between the pulsar and an observer, corresponds to  $\text{HJD}_0=2458374.74535$ . The brightness variation in other bands is consistent with that in the *R*-band. To detect the object at the minimum, we summed all the images obtained close to the phase 0.0. However, we have only obtained a  $3\sigma$  upper limit on its minimum brightness of  $R_{\min} \gtrsim 24.7$ . The respective image is shown in the right panel of Fig. 1.

The coordinate accordance, the coincidence of the photometric and binary periods, and the similarity of the light curve shape to those of other BWs (see Table 5) strongly suggest that the detected variable source is the binary companion of PSR J2052+1219.

The accepted interstellar reddening towards the pulsar  $E(B - V) = 0.08 \div 0.14$  (see Sect. 1) gives Johnson-Cousins

*BVRI* extinction values  $A_B = 0.29 \div 0.44$ ,  $A_V = 0.22 \div 0.33$ ,  $A_R = 0.17 \div 0.26$ , and  $A_I = 0.12 \div 0.18$  for  $R_V = 3.1$  (Schlafly & Finkbeiner 2011). Therefore, the unabsorbed brightness of the source at the maximum is  $R_c \approx 21.8$ . As we noted before, Cromartie et al. (2016) have calculated a minimum companion mass of  $\gtrsim 0.033 M_\odot$  assuming the pulsar mass  $M_{\text{NS}} = 1.35 M_\odot$  and the orbit inclination angle  $i = 90^\circ$ . A corresponding mass function  $f(M_{\text{NS}}, M_2)$  of  $18.78 \times 10^{-6} M_\odot$  is slightly different from the updated value presented by Guillemot, et al. (2019) (see Table 1), while its uncertainty and the uncertainty of the projected semi-major orbit axis still remain unknown. In any case, such a small difference, likely reflecting their uncertainties, does not affect the results of our light curve analysis presented below. For such a low-mass object, the most likely radius value should be about  $\sim 0.1 R_\odot$  (Chabrier et al. 2009). In these old binaries,

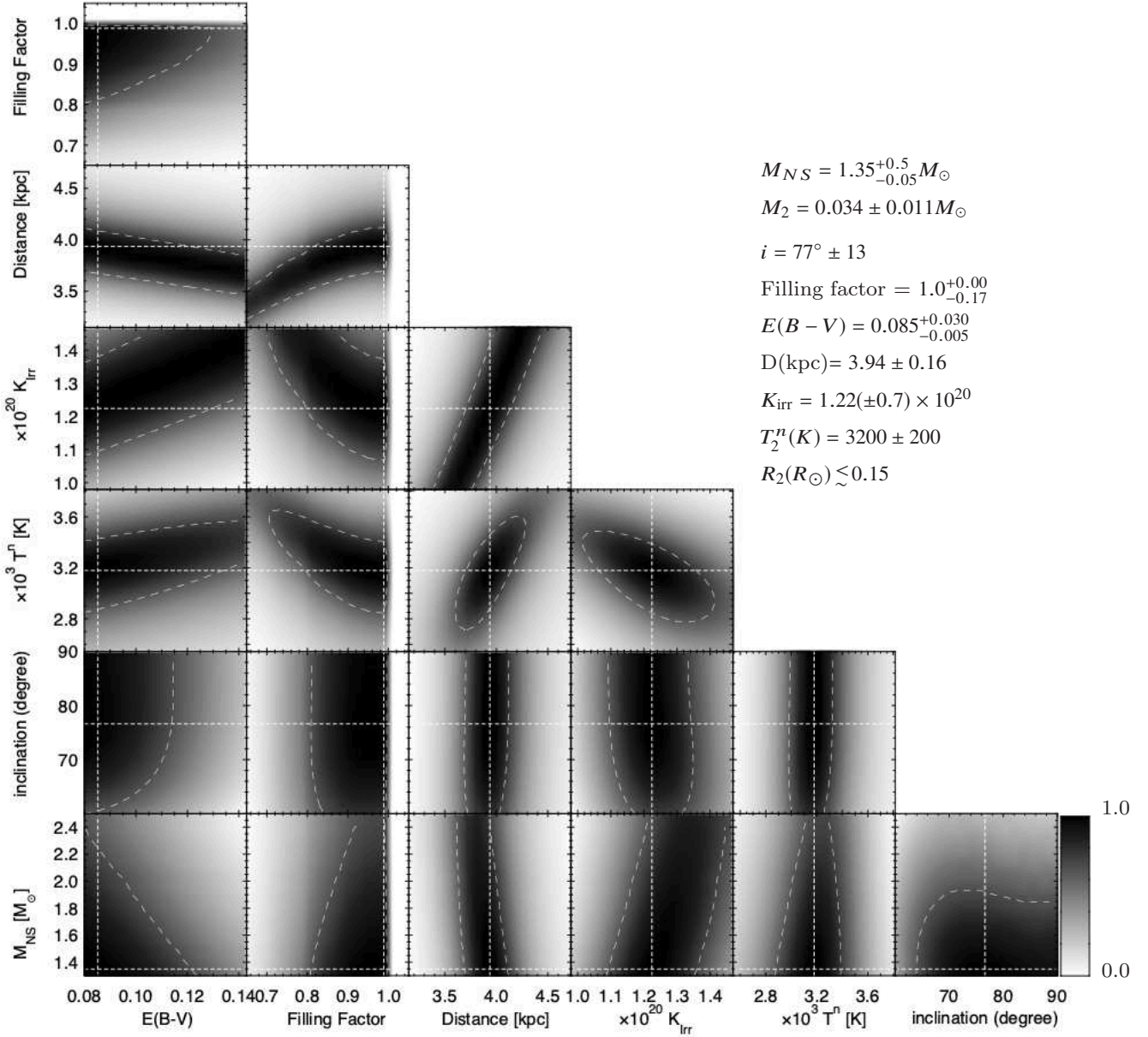


**Figure 3.** Errors of the fit. The black-and-white scale corresponds to the minimum (black) and maximum (white) values of  $\chi^2 = f(\text{par1}, \text{par2})$  in the corresponding plot when other parameters are fixed at the best values. The short-dashed lines correspond to the global minimum of all fitted parameters. The irradiation factor  $K_{\text{irr}}$  is given in  $\text{ergs cm}^{-2} \text{s}^{-1} \text{sr}^{-1}$ . The thin long-dashed lines show the  $1\sigma$  errors of the fit parameters.

the secondary is mainly responsible for the optical radiation. However, such a small object would be very faint and hardly detectable if isolated. This is consistent with the R-band upper limit at the phase 0.0. In close binary MSP systems, the irradiation from the pulsar increases the temperature and luminosity of the front side of the companion and makes it observable at respective orbital phases. For this reason, the strong variability of the detected source is explained by a high temperature difference between the front and the back sides of the secondary.

Unfortunately, the available radio data do not provide information on the duration of the radio emission eclipse in

an orbit. Typically, MSPs in eclipsing binaries are eclipsed for 10–40 per cent of an orbit at 2 GHz, implying the presence of ionised material in a region larger than the Roche lobes of the companions (Archibald et al. 2009). Taking into account this fact and the system parameters, we reproduced the *BVRI*-band light curves using the modelling technique developed by Zharikov et al. (2013). It was designed to include different types of the primary, such as a black hole, a NS, a white dwarf or a main-sequence star, the filling factor of the Roche lobe by the secondary, and possible accretion

**Table 4.** System parameters used for the *BVRI*-band light curve modelling.

Variable and their allowed ranges:
$1.3 < M_{NS} < 2.5$
$0.08 < E(B - V) < 0.14$
R mag (phase=0.0) $\gtrsim 24.7$
$T_2^n$ ; Roche Lobe Filling Factor; Distance
Irradiation Factor $K_{irr}$ , system inclination $i$
Result:
$M_{NS} = 1.35^{+0.5}_{-0.05} M_{\odot}$
$M_2 = 0.034 \pm 0.011 M_{\odot}$
$E(B - V) = 0.085^{+0.030}_{-0.005}$
$T_2^n = 3200 \pm 200$ K
$0.12 < R_2/R_{\odot} \lesssim 0.15$
$0.83 < \text{Roche Lobe Filling Factor} \lesssim 1.0$
D (kpc) = $3.94 \pm 0.16$
$K_{irr} (\text{erg cm}^{-2} \text{ s}^{-1} \text{ sr}^{-1}) = 1.22 (\pm 0.7) \times 10^{20}$
$i = 77.0 \pm 13.0^\circ$
$T_2^{d,min} = 3630$ K $< T_2^d < T_2^{d,max} = 6530$ K (derived)

structures in a binary system. The irradiation of the secondary was taken into account as

$$T_2^d = T_2^n * \left( 1 + \frac{F_{in}}{\Delta S \sigma (T_2^n)^4} \right)^{1/4}, \quad (1)$$

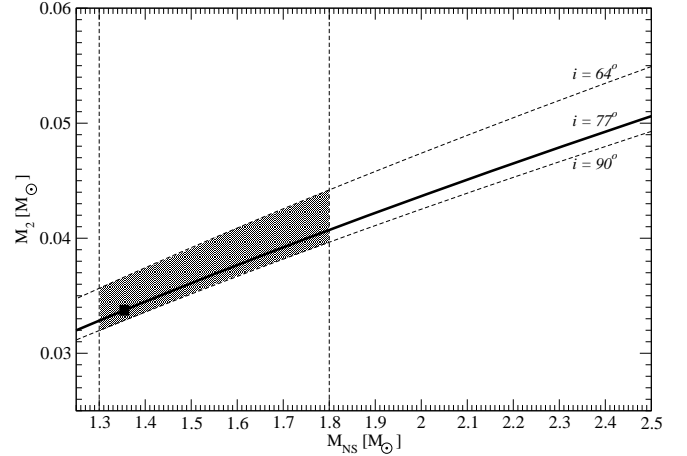
where  $T_2^d$  and  $T_2^n$  are the temperatures of the "day-side" and "night-side" surface element of the secondary, respectively,  $F_{in}$  is the effective heating flux incoming to the "day-side" surface element  $\Delta S$  of the secondary, and  $\sigma$  is the Stefan-Boltzmann constant. The effective heating in our model is defined by the irradiation factor  $K_{irr}$  [ergs s<sup>-1</sup> cm<sup>-2</sup> sr<sup>-1</sup>] as

$$F_{in} = \cos(\alpha_{norm}) \Omega \Delta S K_{irr} \quad (2)$$

where  $\alpha_{norm}$  is the angle between the incoming wind/flux and the normal to the surface element  $\Delta S$ ,  $\Omega = \pi R_{NS}^2/a^2 \approx 1 \times 10^{-9}$  is the solid angle from which the pulsar is visible from the surface element of the companion. The factor  $K_{irr}$  can generally take into account the heating effects caused by a combination of the pulsar thermal emission from the surface of the NS  $\propto \sigma T_{NS}^4$ , its nonthermal radiation of the magnetospheric origin, and the pulsar wind. The last two are proportional to the pulsar spin-down luminosity  $\dot{E}$ . The factor defines the distribution of the temperature on the "day-side" surface elements of the secondary  $T_2^d$ . The MSPs are very old and cold NSs with  $T_{NS} \lesssim 10^5$  and contribution of the thermal emission into the heating can be neglected. In this case, assuming the isotropy of the pulsar wind/radiation,  $K_{irr}$  can be expressed in terms of the measured  $\dot{E}$  and the heating efficiency  $\eta$  of the secondary defined as

$$\eta = \frac{\sum \Delta S \sigma (T_d^4 - T_n^4)}{\dot{E} \pi R^2 / 4 \pi a^2}, \quad (3)$$

where  $a$  is the orbital separation,  $R$  is the polar radius of the secondary and the summation is performed over all surface

**Figure 4.** Mass of the companion vs. mass of the pulsar. The filled area shows the  $1\sigma$  error box of the system parameters. The black square corresponds to the best values of the fit.

elements  $\Delta S$ . Combining equations (1 – 3) yields

$$K_{irr} = \frac{\eta \dot{E}}{4 \pi^2 R_{NS}^2}, \quad (4)$$

assuming that  $R$  is roughly equal to the radius of the secondary neglecting its Roche lobe filling. In case of PSR J2052+1219,  $\frac{\dot{E}}{4 \pi^2 R_{NS}^2} = 5.9 \times 10^{20}$  ergs s<sup>-1</sup> cm<sup>-2</sup> sr<sup>-1</sup> for  $R_{NS} = 12$  km.

To fit the data, we fixed the mass function at the updated value presented in Table 1:

$$f(M_{NS}, M_2) = \frac{(M_2 \sin i)^3}{(M_{NS} + M_2)^2} = 0.00001843 M_{\odot} \quad (5)$$

The variable parameters of the fit were the mass of the pulsar  $M_{NS}$ , the distance, the "night-side" temperature of the secondary  $T_2^n$ , the system inclination  $i$ , the radius  $R_2$  or the Roche lobe filling factor of the secondary, the interstellar absorption  $E(B - V)$ , and the effective irradiation factor  $K_{irr}$ . The mass of the secondary  $M_2$  and the mass ratio  $q \equiv M_2/M_{NS}$  were determined from the equation 5.

The gradient descent method was used to find the minimum of the  $\chi^2$  function defined as

$$\chi^2 = \sum_j^{B,V,R,I} \sum_k^{N_k} \frac{(\text{mag}_k^{\text{obs}} - \text{mag}_k^{\text{calc}})^2}{(\Delta \text{mag}_k^{\text{obs}})^2} \quad (6)$$

with the additional condition that the source is not detected at the phase 0.0 down to  $R \approx 24.7$ .  $N_k$  is the number of the binary phase bins. For each of the observed phases ( $k$ ) the model magnitudes  $\text{mag}_k^{\text{calc}}$  in each band were calculated from the integrated flux  $\sum \Delta S_n \times R_{tr}(\lambda) \times BB_{\lambda}(T)$  of all visible elements of the system, where  $R_{tr}$  is the filter transmission,  $\Delta S_n$  is the projection of the surface element area to the line of sight,  $BB(T)$  is the black body flux from the element. The total flux was converted into the magnitude  $\text{mag}_k^{\text{calc}}$  taking into account the distance to the system, the interstellar extinction, and the band's zero-points. As a first step, the error of the fitting was selected arbitrarily. After the minimum of the functional was reached, we searched for

**Table 5.** Parameters of BW systems detected in the optical. The first column corresponds to the name of the object,  $\Delta m$  is the full amplitude of the optical light curve variation in the corresponding band,  $P_{orb}$  is the orbital period,  $\dot{E}$  is the spin-down luminosity,  $i$  is the system inclination, and the last four columns correspond to the "day-side" and "night-side" temperature estimations, the radius of the companion star and the respective references.

MSP	$\Delta m$	$P_{orb}$ (h)	$\times 10^{34} \dot{E}$ (ergs s <sup>-1</sup> )	inclination degree	$\times 10^3 T_2^d$ (K)	$\times 10^3 T_2^n$ (K)	R (R <sub>⊙</sub> )	Ref.
J1311-3430		1.56	4.9					13
J0636+5128	$\Delta g \approx 2.0$	1.6	0.58	24(2), 40(6)	4.7 3.9	1.7 2.5	0.08 0.10	4, 5
J1518+0204C*	$\Delta F606W > 1.3$	2.1	6.7		3.4-5.3			12
J2051-0827	$\Delta F675W \approx 3.3$	2.38	0.55	~40	4-4.7	< 3		10,15
<b>J2052+1219</b>	$\Delta R > 2.7$	2.8	3.34	77(13)	6.6	3.5	0.14	2
	$\Delta r \gtrsim 4.4$							16
J1544+4937	$\Delta g \approx 2.0$	2.9	1.2	~60	5.4	3.9	0.037	7
J1810+1744	$\Delta g \approx 4.0$	3.6	3.97	48(7)	10.0	3.1	0.15	1,3
J1953+1846A*	$\Delta F606W \approx 3.3$	4.2	1.64	~90				8
J0023+0923	$\Delta g \approx 4.6$	4.8	1.51	58(14)	4.8	2.9	0.05	1
J2256-1024	$\Delta g \approx 5.8$	5.1	3.95	68(11)	4.2	2.5	0.05	1
J0952-0607	$\Delta r \approx 1.6$	6.42	<16.0	~45	4.5-5.8	~2.5		9
J1301+0833	$\Delta g > 2.5$	6.5	7.0	~52	4.6	2.7	<0.1	6
J0610-2100	$\Delta R > 1.7$	6.86	0.23		3.5			14
B1957+20	$\Delta R \approx 5.1$	9.17	16	65(2)	2.9	8.3		11

1-Breton et al. (2013), 2-this paper, 3-Schroeder & Halpern (2014), 4-Kaplan et al. (2018), 5-Draghis & Romani (2018)  
 6-Romani et al. (2016), 7-Tang et al. (2014), 8-Cadelano et al. (2015), 9-Bassa et al. (2017), 10-Stappers et al. (2001),  
 11-Reynolds et al. (2007), 12-Pallanca et al. (2014), 13-Romani et al. (2015), 14-Pallanca et al. (2012), 15-Stappers et al. (1996)  
 16-Draghis et al. (2019)

$\dot{E} = 4\pi^2 I (\dot{P}/P^3)$ , for a moment of inertia  $I = 10^{45}$  g cm<sup>-2</sup>, pulse period  $P$ , and period derivative  $\dot{P}$

\* The intrinsic  $\dot{P}$  and corresponding  $\dot{E}$  can be different from the measured ones due to acceleration in the globular clusters M5 and M71.

the global minimum several times decreasing the acceptable fitting error in the vicinity of the minimum that was reached in the previous step. The search was repeated until the difference between the model and observational light curves became insignificant.

The result of our light curve fitting is presented in Figs. 2, 3, 4, and Table 4. As seen from Fig. 2, the observed light curves are perfectly fitted by the model although the resulting formal reduced  $\chi^2/DOF$  appears to be relatively large (3.54) and the differences between the observed and calculated (O-C) magnitude points reach  $\pm 0.3$  mag. Because the measured magnitude errors are much smaller, the dispersion of the observed points around the model curves is likely caused by an intrinsic stochastic variability of the source at smaller time scales than  $P_b$ , which is not accounted by the model.

To estimate the dependence of the best solution (Table 4) on the fit parameters, we calculated the variation of the  $\chi^2$  functional in the 2D planes (par1, par2) when the other parameters were fixed at the best values (see Figure 3). The grey colour shows the values of  $y \equiv 1/\chi^2$  in the z-scale of  $z = (y - y_{min})/(y_{max} - y_{min})$ . We define the  $1\sigma$  error of the fit as 0.68 from the maxima of the 2D plots. It is marked by the long-dashed lines in Fig. 3.

The fit shows that the object is close to filling its Roche lobe. The obtained distance to the source is  $3.94 \pm 0.16$  kpc, which is in accord with the most recent DM distance estimation based on the YMW16 Galactic electron density model (Sect. 1). The maximum difference between the "day-side" and "night-side" temperatures of the secondary is about 3000 K. The latter is similar to what is observed

in other BW systems. The interstellar extinction derived from the fit,  $E(B - V) = 0.085^{+0.030}_{-0.005}$ , is close to the value proposed by Schlafly & Finkbeiner (2011) at the given distance (see Sect. 1) and it is lower than that predicted by the extinction-distance maps by Green et al. (2018). The masses of the pulsar and its companion are  $1.35^{+0.5}_{-0.05} M_{\odot}$  and  $0.034 \pm 0.011 M_{\odot}$ , respectively. The latter one is only  $\approx 36$  times the Jupiter mass. The system inclination angle  $77 \pm 13^\circ$  indicates that the radio eclipse is most probably related to ionised material escaping from the companion. In Fig. 4, we show the  $1\sigma$  error box of the three parameters in the  $M_{NS} - M_2$  plane. Its sizes are dominated by uncertainties of the optical fit, but not minor uncertainties of the mass function and the projected semi-major axis of the binary orbit mentioned above.

Our best fit model parameters provide the efficiency of the companion heating by the pulsar  $\eta \approx 0.2$ . This value is in agreement with the upper limit on the efficiency of re-radiation  $\lesssim 0.5$  proposed by Ruciński (1969). Discussion of heating mechanisms and their efficiency in binary MSPs can be found in, e.g., Breton et al. (2013); Li et al. (2014); Romani & Sanchez (2016); Deneva et al. (2016) and Sanchez & Romani (2017). Efficiency factors in these systems typically lie in a range of  $\approx 0.1 - 0.3$ . This implies that the relativistic pulsar wind powered by the spin-down luminosity represents an effective factor of heating. However, some objects, e.g., PSR J1810+1744, show  $\eta > 1$ , implying strong anisotropy and/or inhomogeneity of the wind.

In Table 5 we accumulated the observed, derived and modelling parameters of all BW MSPs that were studied via time-resolved optical observations. A correlation is generally

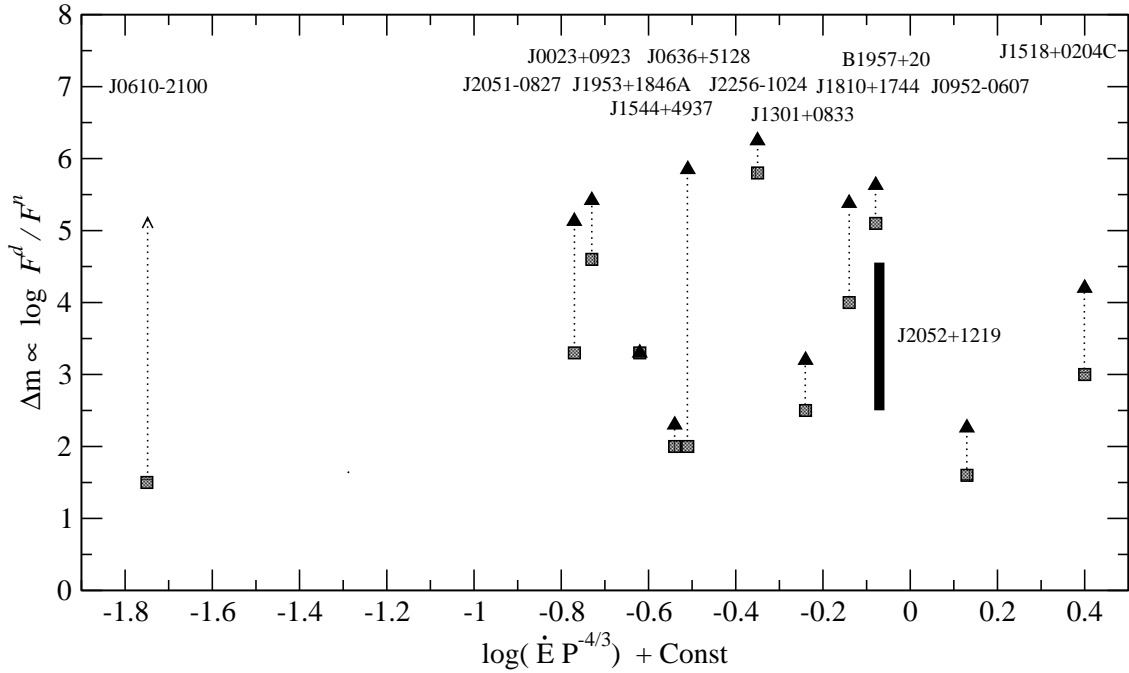


**Figure 5.** Observed amplitudes of magnitude variations vs logarithm of the "spin-down flux"  $\dot{E}P_{orb}^{-4/3}$  for different BWs from Table 5. Squares correspond to the observed amplitudes, and triangles are their values corrected for the systems' inclinations.  $P_{orb}$  is given in hours and  $\dot{E}$  in  $10^{34}$  ergs  $s^{-1}$ . The black rectangle corresponds to PSR J2052+1219.

expected between the brightness variation of the secondary and a "spin-down flux" defined as  $\dot{E}P_{orb}^{-4/3}$ ,

$$\Delta m \propto \log\left(\frac{F_d}{F_n}\right) \propto \log\left(\frac{T_d^4}{T_n^4}\right) \propto \log\left(\eta \frac{\dot{E}}{4\pi a^2}\right) \propto \log(\dot{E}P_{orb}^{-4/3}). \quad (7)$$

In Fig. 5 we show the full amplitude of the optical variations vs logarithm of the "spin-down flux" for BWs with available time-resolved optical photometry (squares). The filled triangles show the total amplitude of the variation corrected for the proposed system inclinations from the cited publications. As seen, there is no evident correlation between the "spin-down flux" and  $\Delta m \propto (T_d/T_n)^4$  at a scale of about two orders of the "spin-down flux". Therefore, the origin of the "day-side" heating appears to be more complicated than suggested by Eq 7. As the pulsar wind is anisotropic, it is very likely that the heating effect highly depends on the unknown pulsar spin axis inclination. Moreover, it is possible that it is not only the pulsar wind that drives the heating. Specific structures of the surface magnetic field and possible convective zones of the secondary can also affect the observed optical variations of different BW companions.

#### 4 CONCLUSION

We have presented the optical identification and time-resolved multi-band photometry of the BW PSR J2052+1219. The detected object shows a strong optical variability with the period  $P = 2.752h$ , which coincides with the system orbital period reported by Cromartie et al. (2016) and derived from the radio timing data. We reproduced the object light curve using the model of the heating of the companion star by the pulsar. As a

result, we independently estimated the distance to the system of  $\approx 4$  kpc which is in accord with the dispersion measure distance based on the Galactic electron density model by Yao et al. (2017). The companion mass is only  $0.034 \pm 0.011M_{\odot}$  or about 36 times the Jupiter mass  $M_J$ . Its radius is  $\approx 0.15R_{\odot}$  or only by a factor of 1.5 larger than the Jupiter radius  $R_J$ . It is close to filling its Roche lobe, and it has a gradient of the surface temperature of about 3000 K between the side facing the pulsar ( $\sim 6500K$ ) and the back side ( $\sim 3200K$ ). For comparison, brown dwarfs with similar masses typically have radii of about  $R_J$  (see, e.g., Bayliss, et al. 2017) and lower effective temperatures of  $\lesssim 2800$  K (Helling & Casewell 2014). We can speculate that as the system evolves, the companion can transform into a brown dwarf or a planet. At the current stage, its larger size and temperature are unconditionally determined by the pulsar wind. The presence of eclipse in the radio together with the  $R$ -band upper limit at the minimum brightness orbital phase imply a high inclination of the system. This is supported by our estimation of the inclination angle of  $77^{\circ} \pm 13$  following from the optical light curve fit. The estimated heating efficiency of the companion by the pulsar is  $\eta \approx 0.2$ , similar to that observed in other BW systems. Maximum deviations of individual observational optical points from the model light curve reach  $\approx 20$  per cent. They can be likely attributed to the intrinsic short-time variations of the companion caused by complex plasma behaviors near the companion surface due to anisotropy and/or inhomogeneity of the pulsar wind. Overall, PSR J2052+1219 is of a particular interest for further spectroscopic and fast photometric studies using large telescopes.

We note that when this paper was submitted, Draghis et al. (2019) have published optical light curves of the considered system independently obtained with Keck,



SOAR, and MDM telescopes. Their fit results including the companion night side temperature and mass, and the distance to the system are consistent with the values obtained by us, while the inclination angle of the orbit is significantly lower, about  $54^\circ$ . Considering such a small inclination, it may be difficult to explain the pulsar eclipse accounting for a small radius of the companion. Draghis et al. (2019) do not constrain from their fit  $E(B - V)$ , the day-side temperature, the radius of the companion, its Roche-lobe filling factor, and the mass of the NS, fixing it at  $1.5M_\odot$ .

## ACKNOWLEDGEMENTS

We are grateful to the anonymous referee for useful comments which improved the paper. We thank F. Camilo, H. T. Cromartie and M. Roberts for providing the information from the radio timing measurements. J.S.D. was supported by the NASA Fermi program. SZ and AK acknowledge PAPIIT grant IN-100617 for resources provided towards this research. The work of DZ and AK was funded by RFBR according to the research project 18-32-20170. The work of YS was partially supported by the RFBR grant 16-29-13009. Based upon observations carried out at the Observatorio Astronómico Nacional on the Sierra San Pedro Mártir (OAN-SPM), Baja California, México. This work has made use of data from the European Space Agency (ESA) mission *Gaia* (<https://www.cosmos.esa.int/gaia>), processed by the *Gaia* Data Processing and Analysis Consortium (DPAC, <https://www.cosmos.esa.int/web/gaia/dpac/consortium>). Funding for the DPAC has been provided by national institutions, in particular the institutions participating in the *Gaia* Multilateral Agreement. The Pan-STARRS1 Surveys (PS1) and the PS1 public science archive have been made possible through contributions by the Institute for Astronomy, the University of Hawaii, the Pan-STARRS Project Office, the Max-Planck Society and its participating institutes, the Max Planck Institute for Astronomy, Heidelberg and the Max Planck Institute for Extraterrestrial Physics, Garching, The Johns Hopkins University, Durham University, the University of Edinburgh, the Queen's University Belfast, the Harvard-Smithsonian Center for Astrophysics, the Las Cumbres Observatory Global Telescope Network Incorporated, the National Central University of Taiwan, the Space Telescope Science Institute, the National Aeronautics and Space Administration under Grant No. NNX08AR22G issued through the Planetary Science Division of the NASA Science Mission Directorate, the National Science Foundation Grant No. AST-1238877, the University of Maryland, Eotvos Lorand University (ELTE), the Los Alamos National Laboratory, and the Gordon and Betty Moore Foundation.

## REFERENCES

Alpar M. A., Cheng A. F., Ruderman M. A., Shaham J., 1982, *Natur*, 300, 728  
 Archibald A. M., et al., 2009, *Sci*, 324, 1411  
 Bassa C. G., et al., 2017, *ApJ*, 846, L20  
 Bayliss D., et al., 2017, *AJ*, 153, 15  
 Bisnovatyi-Kogan G. S., Komberg B. V., 1974, *SvA*, 18, 217

Breton R. P., et al., 2013, *ApJ*, 769, 108  
 Burgay M., et al., 2006, *MNRAS*, 368, 283  
 Cadellano M., et al., 2015, *ApJ*, 807, 91  
 Chabrier G., Baraffe I., Leconte J., Gallardo J., Barman T., 2009, *AIPC*, 1094, 102  
 Cordes, J. M., & Lazio, T. J. W. 2002, arXiv:astro-ph/0207156  
 Cromartie H. T., et al., 2016, *ApJ*, 819, 34  
 Deeming T. J., 1975, *Ap&SS*, 36, 137  
 Deneva J. S., et al., 2016, *ApJ*, 823, 105  
 Draghis P., Romani R. W., 2018, *ApJ*, 862, L6  
 Draghis P., Romani R. W., Filippenko A. V., Brink T. G., Zheng W., Halpern J. P., Camilo F., 2019, arXiv, arXiv:1908.00992  
 Flewelling, H. A., Magnier, E. A., Chambers, K. C., et al. 2016, arXiv:1612.05243  
 Fruchter A. S., Stinebring D. R., Taylor J. H., 1988, *Natur*, 333, 237  
 Gaia Collaboration, et al., 2016, *A&A*, 595, A1  
 Gaia Collaboration, et al., 2018, *A&A*, 616, A1  
 Green G. M., et al., 2018, *MNRAS*, 478, 651  
 Guillemot L., et al., 2019, arXiv, arXiv:1907.09778  
 Kaplan D. L., Stovall K., van Kerkwijk M. H., Fremling C., Istrate A. G., 2018, *ApJ*, 864, 15  
 Kostov A., Bonev T., 2018, *BlgAJ*, 28, 3  
 Landolt A. U., 1992, *AJ*, 104, 340  
 Li M., Halpern J. P., Thorstensen J. R., 2014, *ApJ*, 795, 115  
 Helling C., Casewell S., 2014, *A&ARv*, 22, 80  
 Li K.-L., Kong A. K. H., Hou X., Mao J., Strader J., Chomiuk L., Tremou E., 2016, *ApJ*, 833, 143  
 Lindegren L., et al., 2018, *A&A*, 616, A2  
 Manchester R. N., Hobbs G. B., Teoh A., Hobbs M., 2005, *AJ*, 129, 1993  
 Pallanca C., Mignani R. P., Dalessandro E., Ferraro F. R., Lanzoni B., Possenti A., Burgay M., Sabbi E., 2012, *ApJ*, 755, 180  
 Pallanca C., Ransom S. M., Ferraro F. R., Dalessandro E., Lanzoni B., Hessels J. W. T., Stairs I., Freire P. C. C., et al., 2014, *ApJ*, 795, 29  
 Ray, P. S., Abdo, A. A., Parent, D., et al. 2012, arXiv:1205.3089  
 Reynolds M. T., Callanan P. J., Fruchter A. S., Torres M. A. P., Beer M. E., Gibbons R. A., 2007, *MNRAS*, 379, 1117  
 Romani R. W., Filippenko A. V., Silverman J. M., Cenko S. B., Greiner J., Rau A., Elliott J., Pletsch H. J., 2012, *ApJ*, 760, L36  
 Romani R. W., Filippenko A. V., Cenko S. B., 2015, *ApJ*, 804, 115  
 Romani R. W., Graham M. L., Filippenko A. V., Zheng W., 2016, *ApJ*, 833, 138  
 Romani R. W., Sanchez N., 2016, *ApJ*, 828, 7  
 Ruciński S. M., 1969, *AcA*, 19, 245  
 Sanchez N., Romani R. W., 2017, *ApJ*, 845, 42  
 Schlegel D. J., Finkbeiner D. P., Davis M., 1998, *ApJ*, 500, 525  
 Schlafly E. F., Finkbeiner D. P., 2011, *ApJ*, 737, 103  
 Schroeder J., Halpern J., 2014, *ApJ*, 793, 78  
 Schuster, W. J., & Parrao, L. 2001, *Rev. Mex. Astron. Astrofis.*, 37, 187  
 Schuster, W. J., Parrao, L., & Guichard, J. 2002, *Journal of Astronomical Data*, 8  
 Stappers B. W., Bessell M. S., Bailes M., 1996, *ApJ*, 473, L119  
 Stappers B. W., van Kerkwijk M. H., Bell J. F., Kulkarni S. R., 2001, *ApJ*, 548, L183  
 Tang S., et al., 2014, *ApJ*, 791, L5  
 Tonry J. L., et al., 2012, *ApJ*, 750, 99  
 van den Heuvel E. P. J., van Paradijs J., 1988, *Natur*, 334, 227  
 van Dokkum P. G., 2001, *PASP*, 113, 1420  
 Wadiasingh Z., Harding A. K., Venter C., Böttcher M., 2015, *salt.conf*, 75  
 Zharikov S. et al., 2013, *A&A*, 549, A77  
 Zharikov S., Mignani R. P., 2013, *MNRAS*, 435, 2227

10 *S. Zharikov, A. Kirichenko, D. Zyuzin et al.*

Yao J. M., Manchester R. N., Wang N., 2017, ApJ, 835, 29